

# Journal of Materials Chemistry A

Accepted Manuscript



This is an *Accepted Manuscript*, which has been through the Royal Society of Chemistry peer review process and has been accepted for publication.

*Accepted Manuscripts* are published online shortly after acceptance, before technical editing, formatting and proof reading. Using this free service, authors can make their results available to the community, in citable form, before we publish the edited article. We will replace this *Accepted Manuscript* with the edited and formatted *Advance Article* as soon as it is available.

You can find more information about *Accepted Manuscripts* in the [Information for Authors](#).

Please note that technical editing may introduce minor changes to the text and/or graphics, which may alter content. The journal's standard [Terms & Conditions](#) and the [Ethical guidelines](#) still apply. In no event shall the Royal Society of Chemistry be held responsible for any errors or omissions in this *Accepted Manuscript* or any consequences arising from the use of any information it contains.

## High electrochemical performance and phase evolution of magnetron sputtered MoO<sub>2</sub> thin films with hierarchical structure for Li-ion battery electrodes

Yulong Liu<sup>a</sup>, Hong Zhang<sup>a\*</sup>, Pan Ouyang<sup>a</sup>, Wenhao Chen<sup>a</sup>, Ying Wang<sup>a</sup>, Zhicheng Li<sup>a,b,\*</sup>

**Abstract:** MoO<sub>2</sub> thin films with hierarchical structure were magnetron-sputtering deposited on copper foils by using a metal molybdenum target. The microstructure, electrochemical performance and phase evolution of the MoO<sub>2</sub> thin films were investigated. The novel structure contributes to the high specific capacity of 860 mA h g<sup>-1</sup> at a current rate of 400 mA g<sup>-1</sup>, high reversible capacity of 760 mA h g<sup>-1</sup> after 100 cycles and high rate capability (370 mA h g<sup>-1</sup> at 3200 mA g<sup>-1</sup>). The electrochemical mechanism were studied by investigating the microstructures and phase evolution of the MoO<sub>2</sub> thin film electrodes by using the transmission electron microscopy (TEM) after being electrochemically induced at various stages in the first charge-discharge cycle and in 12<sup>th</sup> cycle, respectively. The TEM investigations reveal that the MoO<sub>2</sub> thin film electrodes undergo a conversion reaction such as  $\text{MoO}_2 + x\text{Li}^+ \leftrightarrow \text{Li}_x\text{MoO}_2 \leftrightarrow \text{Mo} + x\text{Li}_2\text{O}$ , which is kinetically infeasible under normal condition.

### 1 Introduction

Lithium ion batteries (LIBs), for their high energy density and long cycle life, have been widely applied in portable electronics and hold bright prospect as energy

---

<sup>a</sup>School of Materials Science and Engineering, Central South University, Changsha 410083, P.R. China. E-mail: zhchli@csu.edu.cn, hzhang@csu.edu.cn

<sup>b</sup>State Key Laboratory of Powder Metallurgy, Central South University, Changsha 410083, P.R. China

storage devices for electric vehicles.<sup>[1,2]</sup> However, it is greatly hindered by the current available carbonaceous materials as the anode for the limited capacity (*e.g.*, 372 mA h g<sup>-1</sup> for graphite) and safety issues related to Li plating.<sup>[3]</sup> To surmount the drawbacks of low energy and power density of graphite, seeking alternative anode materials with superior performance has become an urgent task to meet the challenges of emerging green economical markets.<sup>[4]</sup> Nanoscale transition metal oxides such as MoO<sub>2</sub>, Fe<sub>3</sub>O<sub>4</sub>, Co<sub>3</sub>O<sub>4</sub>, NiO and Mn<sub>3</sub>O<sub>4</sub>, *etc.*, are capable of uptaking more than one lithium and exhibiting significantly high theoretical capacities and outstanding electrochemical performance.<sup>[5-9]</sup>

MoO<sub>2</sub> has recently attracted considerable attention due to its high theoretical reversible capacity (838 mA h g<sup>-1</sup>) and relatively higher Li insertion potential than that of carbonaceous materials.<sup>[10-16]</sup> Unfortunately, practical application of bulk MoO<sub>2</sub> is limited by slower kinetics, which inhibits the redox conversion reaction that is thermodynamic feasible under normal conditions.<sup>[17-19]</sup> Synthesizing well designed MoO<sub>2</sub> structures with enhanced diffusion kinetics has been proved efficient to overcome the drawbacks.<sup>[16,20]</sup> The excellent lithium storage performance of ultrafine particles over bulk counterparts can be ascribed to shorter solid-state diffusion length for charge carrier transfer and larger electrode/electrolyte contact area.<sup>[21-23]</sup>

Although the MoO<sub>2</sub> electrodes with different morphologies have been reported,<sup>[12, 14-16, 24]</sup> to our knowledge, there has been little report on the thin film electrode with long cycle life and high rate capability so far. Fabricating binder-free and carbon-free thin film electrode benefits the merits of low-cost, high energy power, and long cycle

life.<sup>[25-27]</sup> In addition, thin films deposited on electronically conductive substrates (*e.g.* Cu foil) are more suitable for fundamental electrochemical studies of the transition metal oxides, avoiding the interference from the additives in polymer-bonded electrodes.<sup>[28]</sup> Where, sputtering is an effective method to deposit thin film electrodes and has demonstrated its potential in preparing nanostructured electrodes for all solid state thin film LIBs, which can be used in microelectronic mechanical systems (MEMS) and small size electronic devices.<sup>[29-33]</sup>

Additionally, full understanding of the electrochemical characteristics taking place during charge/discharge processes can provide strategies to improve the lithium storage performance. A number of techniques, such as X-ray diffraction (XRD),<sup>[34]</sup> Raman spectroscopy,<sup>[35]</sup> scanning electron microscopy (SEM)<sup>[36]</sup> and transmission electron microscopy (TEM), *etc.*, have been developed to investigate phase and microstructure evolution during electrochemical cycling.

Herein, MoO<sub>2</sub> deposited on Cu foils by radio-frequency (RF) magnetron sputtering were prepared. The electrochemical performance and microstructure evolution of thin film electrodes were evaluated.

## 2 Experimental

### 2.1 Sample preparation

MoO<sub>2</sub> thin films were obtained by RF reaction sputtering of Mo target (99.9%) onto square Cu foil substrates (the size of 10 mm × 10 mm) by using a magnetron sputtering system (JGP 450, China) at room temperature. During deposition, the

substrate holder was rotating at a speed of 30 rpm in order to enhance the homogeneity of thin film. The sputtering chamber was evacuated below  $5.0 \times 10^{-4}$  Pa with a mechanical pump and turbo-molecular pump as the base pressure. The pressure of mixture ambient gas Ar/O<sub>2</sub>, with constant flows of 32 sccm and 8 sccm, was controlled at 0.6 Pa by a needle valve. The sputtering power was about 80 W, and the distance between substrate and target was about 70 mm. The deposition time was 60 min after pre-sputtering the target for 30 min to remove contamination on the target surface. The weight of each piece of thin film was obtained to be about 0.25 mg by subtracting the substrate weight from the total weight of the thin film on Cu foil, which was examined by an electronic analytical balance (Ohaus Discovery, with resolution of 0.01 mg, American).

## 2.2 Phase and microstructure characterization

The morphologies and microstructures of the thin films were characterized by using a field-emission scanning electron microscopies (FE-SEM) (FEI Nova NanoSEM 230 and Sirion 200), and a transmission electron microscopy (TEM) (FEI Tecnai G<sup>2</sup> F20) operating at 200 kV. The TEM specimens of the as-deposited thin film on Cu foils were prepared by ion milling with a precision ion milling system (Gatan 691). The phase component of the as-deposited MoO<sub>2</sub> thin film on silicon substrate were investigated by using a Rigaku D/MAX 2500 diffractometer with Cu K $\alpha$  radiation ( $\lambda = 0.154056$  nm) at a step of 0.02°. And the electronic state and the composition of the as-deposited thin film on glass was investigated by using X-Ray

photoelectron spectroscopy (XPS) conducted on a K-Alpha 1063 instrument with monochromated Al-K $\alpha$  as the X-ray source.

For the post-mortem TEM analyses, the sample that had been electrochemically induced at a designated potential was kept until the current less than 10  $\mu$ A, then the thin film electrode was disassembled and rinsed with anhydrous Dimethyl carbonate (DMC) to eliminate the residual Li salts. After that, the active materials were scratched down from the Cu foil substrate and made a suspension with acetone. The resulting loosen powder was then transferred from the suspension to the holey carbon TEM grid and dried for the TEM observation.

### 2.3 Electrochemical analyses

The as-deposited samples were kept at 120 °C in a vacuum oven overnight. The two-electrode 2032 coin cells (Li/electrolyte/MoO $_2$ ) were assembled in the glove box filled with ultra-high purity nitrogen (MBraun Glove Box). Polypropylene membrane (Celgard 3501) was used as a separator, lithium metal foil was used as a reference and counterpart electrode, and 1.0 mol L $^{-1}$  LiPF $_6$  in mixed ethylene carbonate (EC) and diethyl carbonate (DEC) (the weight ratio of EC to DEC is 1:1) as the electrolyte. The galvanostatic charge/discharge measurements of the MoO $_2$  based thin film electrodes were performed with a battery measurement system (Land CT2001A, China) at room temperature. The assembled cells were tested with a voltage cut-off range of 0.01-3 V vs. Li/Li $^+$  at various charging rates. Cyclic voltammetry (CV) performances of electrodes were determined by an electrochemical workstation (Gamry Reference600,

USA) in the voltage range of 0.01-3 V at a scan rate of 0.1 mV s<sup>-1</sup>.

### 3 Results and discussion

#### 3.1 Microstructure characterization of as-deposited MoO<sub>2</sub>

Fig. 1 shows the SEM observations of the as-deposited MoO<sub>2</sub> thin film on the Cu foil substrate. Cu foil substrate, as shown in the inset (a) in Fig. 1, exhibits nodule type structure with numerous micrometered columns. Inheriting the rough surface characteristics of the substrate, the as deposited MoO<sub>2</sub> thin film exhibits island-chain like morphology as shown in the inset (b) in Fig. 1, a secondary electron image with a tilting angle of 52°. Enlarged view of the cauliflower like humps, as shown in the inset (c) in Fig. 1, reveals that a single floret (island) is an aggregation of nano-sized particles (about 200 nm). The inset (d) shows a cross-sectional SEM observation of the as-deposited MoO<sub>2</sub> thin film. It can be seen that the thickness of the film is about 1 μm, adhering to the Cu substrate firmly. From the SEM observations in Fig. 1, it is interesting to emphasize that each island is a cauliflower like humps with a size range of 2-5 μm, and the grooves between two islands can act as channels for lithium ion transfer into/out, thus enhancing the kinetic capability. This kind of structure could effectively release stress caused by volume changes in order to prevent the detachment of electrode from current collector, thereby maintaining the electron-contacting channels.<sup>[37]</sup>

Fig. 2a shows an XRD spectrum of the as-deposited MoO<sub>2</sub> thin film on silicon substrate. For comparison, the XRD spectra of hydrothermal synthesized MoO<sub>2</sub><sup>[9, 22]</sup>

and sintered MoO<sub>2</sub> ceramic are insert and some of the diffraction peaks were indexed. One can see that the diffraction peaks of the as-deposited thin film at 36.9 ° and 41.8 ° matches the ones of the monoclinic structured MoO<sub>2</sub> (PDF no. 65-5787, space group of P2<sub>1</sub>/c, lattice parameters of  $a=0.5611$  nm,  $b=0.4856$  nm,  $c=0.5628$  nm,  $\beta=120.95^\circ$ ). This indicates that the MoO<sub>2</sub> thin film was obtained.

XPS was employed to analyze the electronic state and the composition of the as-deposited thin film on glass substrate in present investigation. A typical survey XPS spectrum is shown in Fig. 2b. The XPS spectrum involves the distinct peaks at 234.1 eV (Mo 3d), 399.1 eV (Mo 3p<sub>3/2</sub>), 416.2 eV (Mo 3p<sub>1/2</sub>), and 532.1 eV (O 1s), which are in accordance with that characteristic of MoO<sub>2</sub>.<sup>[9]</sup> The signal of Mo 3d is further investigated by a high resolution XPS as shown in Fig. 2c. The XPS binding energies of the Mo 3d<sub>5/2</sub> and Mo 3d<sub>3/2</sub> are 229.4 eV and 232.6 eV, respectively, and they belong to the Mo (IV) oxidation state of MoO<sub>2</sub>.<sup>[38]</sup> Meanwhile, the doublet at 232.6 eV for Mo (VI) 3d<sub>5/2</sub> and 235.8 eV for Mo (VI) 3d<sub>3/2</sub> are also detected and should arise from the possible surface oxidation of the MoO<sub>2</sub> in air.<sup>[9, 38, 39]</sup>

Fig. 3a shows a typical TEM observation of the as-deposited MoO<sub>2</sub> thin film, nano domains with average size of 5 nm densely distributed. While the selected area electron diffraction (SAED) pattern, as inset in Fig. 3a, is composed of the concentric diffraction rings from the monoclinic MoO<sub>2</sub> phase. The diffraction rings could be indexed to the {011}, { $\bar{2}$  11}, { $\bar{2}$  12}, { $\bar{1}$  22}, { $\bar{4}$  02}, { $\bar{1}$  33} and {033} crystal planes of the MoO<sub>2</sub> phase, respectively. High resolution TEM (HRTEM) observation, as shown in Fig. 3b, also reveals that the thin film contains homogenous dispersed MoO<sub>2</sub>

nano domains, among which are amorphous phase that might buffer volume changes during the electrochemical reaction. Two lattice fringes in one of the domain corresponding to (200) and (012) crystal planes of monoclinic MoO<sub>2</sub> are indexed; while the other two lattice fringes belongs to (200) and (002) planes can also be detected as shown in this figure.

Through the careful microstructure investigations, it is reasonable to assume that the as-deposited MoO<sub>2</sub> thin film possesses hierarchical structure, *i.e.*, a great deal of micro-sized cauliflower-like humps composed of hundreds of nano-sized particles with dispersed nano domains and disordered domain boundaries. This kind of structure feature possesses merits of binder and carbon additive free, higher surface area for flux of the electrolyte, grooves and gaps for lithium ion immersion and transport, rigid contact to the current collector for excellent electronic conductivity. All of these will improve the electrochemical performance of the thin film electrode.

### 3.2 Electrochemical performance

To get insight into the electrochemical performance of thin film electrode, cyclic voltammetry measurements were carried out at a scan rate of 0.1 mV s<sup>-1</sup> in the voltage range 0.01-3 V. Fig. 4 presents the 1<sup>st</sup>, 2<sup>nd</sup>, 5<sup>th</sup>, 100<sup>th</sup> cyclic voltammograms (CVs) of a MoO<sub>2</sub> thin film electrode. The thin film exhibits a different reduction and oxidation performance in the first cycle compared to the subsequent cycles. There are several reduction peaks in the first cycle while only two reduction peaks can be observed in the subsequent ones and their peak positions are distinct from each other. More

specifically, during the first cycle, reversible  $\text{Li}^+$  uptake/removal takes place at 1.0-2.0 V, whereas, irreversible peaks at two voltage regions (above 2.0 and below 1.0 V) and that appearing at below 1.0 V may be related to inevitable formation of passivating solid surface film (SEI) on the electrode in the first cycle.<sup>[40]</sup> Two redox couples at 1.09/1.42 V and 1.4/1.9 V are associated with the reversible phase transition (monoclinic-orthorhombic-monoclinic) of partially lithiated  $\text{Li}_x\text{MoO}_2$  as suggested by Dahn *et al.*<sup>[41]</sup> The positions of redox peaks do not change in the subsequent cycles even after 100 cycles as shown in Fig. 4, indicating the high reversibility of phase transitions. This high reversibility takes the advantages of the hierarchical microstructure of the thin film electrode. Interestingly, an evident small redox couples at 0.4/0.5 V emerge in the subsequent cycles, mainly corresponding to a more complete conversion from  $\text{MoO}_2$  to metallic Mo and  $\text{Li}_2\text{O}$  after the initial activated process.<sup>[16, 20]</sup> This phenomenon could be further supported by charge-discharge profile, 75% capacity of thin film electrode is mainly derived from a lower voltage range below 0.5 V as shown in Fig. 5a.

Fig. 5a shows the representative galvanostatic discharge and charge profiles of the  $\text{MoO}_2$  thin film electrode recorded in the range of 0.01-3 V, at a current rate of 400  $\text{mA g}^{-1}$  ( $100 \mu\text{A cm}^{-2}$ ). The initial discharge and charge capacities are respectively 1264 and 883  $\text{mA h g}^{-1}$ , *i.e.*, the related capacities can also be determined to be 0.316  $\text{mA h cm}^{-2}$  and 0.221  $\text{mA h cm}^{-2}$  in the area specific capacities, respectively. The irreversible capacity loss is of about 30% during the first discharge/charge cycle. The high irreversible capacity loss may result from the decomposition of electrolyte and

the formation of the SEI film,<sup>[40]</sup> which consume a large amount of lithium in the first cycle and also consistent with the CV results in Fig. 4.

It is observed that the lithiation process of MoO<sub>2</sub> is divided into several stages. As shown in the first discharge curves in Fig. 5a, small plateaus are observed at above 2.0 V, 1.4 V and long plateau at below 0.5 V, which are consistent with the previous CV results. The high voltage plateaus (about 2.0 V) could be attributed to the insertion of lithium ion into inner structure of Mo-O layers,<sup>[42, 43]</sup> while the plateaus in the range of 1.3-1.4 V are related to the phase transformation as indicated in CV. The low potential plateau (below 0.5 V) should assign to the conversion reaction to the formation of metallic Mo and Li<sub>2</sub>O, and the irreversible SEI films.<sup>[40]</sup> From the second cycle onwards, discharge curves are similar to each other. The phase transition related plateaus between 1.1-1.5V and long plateau at potential less than 0.5 V are observed, and the total capacity mainly comes from the low potential region. Such a low potential plateau is considerable for practical applications as an anode in LIBs. Based on the CV results and charge/discharge profiles, the reactions of the MoO<sub>2</sub> thin film could be described as following:  $\text{MoO}_2 + x\text{Li}^+ \leftrightarrow \text{Li}_x\text{MoO}_2 \leftrightarrow \text{Mo} + x\text{Li}_2\text{O}$ .<sup>[9, 16, 20]</sup>

To further confirm aforementioned stepwise lithiation process, differential capacity curves are presented in Fig. 5b. The peaks in the whole potential range are in good agreement with the CV results (see in Fig. 4) and discharge/charge curves (Fig. 5a). For example, the two irreversible peaks at high potential around 2.0 V in the first cycle and then disappeared in the subsequent cycles. The other reversible redox peaks appear in the medium potential region (1.1-1.5 V) and low potential region (below 0.5

V). These peaks kept until the 100<sup>th</sup> cycle, as shown in Fig. 5b, showing excellent reversibility of the thin film electrode. These further confirm the lithiation mechanism as mentioned above.

The cycling performance of the MoO<sub>2</sub> thin film electrode at a current rate of 400 mA g<sup>-1</sup> is shown in Fig. 5c. The capacity of MoO<sub>2</sub> thin film electrode experienced a drop before gradually rising to a high value of 860 mA h g<sup>-1</sup> in the 46<sup>th</sup> cycle. This phenomenon might be attributed to an activated process. Dynamically, Li ions need time to transport and diffuse inside the particles and at the same time the mean free path of Li-ion in solid is smaller compared with the particle size. In addition, it is noteworthy that the reversible capacities are a little higher than the theoretical capacity of MoO<sub>2</sub>. The extra capacity (20 mAh g<sup>-1</sup> in 46<sup>th</sup> cycle) might result from the interfacial Li storage.<sup>[44, 45]</sup> A high specific capacity of 762 mA h g<sup>-1</sup> is retained after 100 cycles, illustrating a high stability of Li uptake/removal process in the MoO<sub>2</sub> thin film electrode. This performance can be comparable with previous reported MoO<sub>2</sub> electrode,<sup>[9, 10, 46-49]</sup> and this capacity is still more than twice of the theoretical specific capacity of 372 mA h g<sup>-1</sup> of the commercial graphite.

In order to fully estimate the excellent cycle performance of the MoO<sub>2</sub> thin film electrode, the rate capability under high current densities are investigated. As the charge/discharge rates are increased from 400 mA g<sup>-1</sup> to 800 mA g<sup>-1</sup>, 1600 mA g<sup>-1</sup> and 3200 mA g<sup>-1</sup>, the capacities of the MoO<sub>2</sub> thin film electrode decrease from 796 to 707, 480 and 330 mA h g<sup>-1</sup>, respectively (as shown in Fig. 5d). As the cell was reset to work at the current density of 400 mA g<sup>-1</sup> after the rate performance measurements,

the cell still maintained a high capacity of  $730 \text{ mA h g}^{-1}$ . The electrode demonstrates superior high rate performance and long-time cycling stability to that of  $\text{MoO}_2$  graphene thin film electrode prepared by Xia *et al.*<sup>[46]</sup> The superior high rate capability and excellent cycling performance of the electrode could attribute to the novel structure of the deposited  $\text{MoO}_2$  thin film. As one can see in the SEM (Fig. 1) and TEM (Fig. 3) images, the good integrity and adhesion to the Cu foil current collector guarantee good electronic conductivity during the discharge/charge processes, the smaller domain size can effectively reduce the diffusion distance of  $\text{Li}^+$  ions and electrons, the grooves can act as a buffer to accommodate volume changes during the repeated discharge and charge processes.

### 3.3 Phase evolution during electrochemical processes

Full revealing of the electrochemical processes taking place in batteries continues to be of great interest. The understanding of microstructure evolution of oxide anodes during cycling can provide strategies to improve the lithium storage performance. Thus, the cells applied in the electrochemical performance test were disassembled and the reaction products were harvested and analyzed by TEM. The TEM investigations were performed when the electrodes were discharged to the points of 1.3 V and 0.01 V, and those were charged to 1.6 V and 3 V in the first cycle, respectively.

A typical TEM observation of the electrode discharged to 1.3 V in the first cycle is shown in Fig. 6a. The corresponding SAED pattern (right-up inset) can be assigned to the monoclinic  $\text{Li}_{0.98}\text{MoO}_2$  (PDF no. 84-0603, space group of  $P2_1/c$ , lattice

parameters of  $a = 0.55629$  nm,  $b = 0.5205$  nm,  $c = 0.5855$  nm,  $\beta = 118.796^\circ$ ) and the diffraction rings can be indexed as the crystal planes of  $\{011\}$ ,  $\{002\}$  and  $\{\bar{2}12\}$ , respectively. In addition, a set of lattice fringe with the spacing of  $\sim 0.34$  nm, which assigned to the  $\{011\}$  plane of intermediate  $\text{Li}_{0.98}\text{MoO}_2$  phase can be detected from the HRTEM image (left-down inset in the Fig. 6a). The results confirm that the intermediate phase  $\text{Li}_{0.98}\text{MoO}_2$  emerges. This is in agreement with the CV analysis at 1.3 V in Fig. 3. The related electrochemical reaction can be described as Eq. (1):



A TEM investigation of the electrode discharged to 0.01 V in the first cycle is shown in Fig. 6b. Three diffraction rings, right-up inset, can be assigned to  $\text{Li}_2\text{O}$  structure (PDF no. 12-0254, space group  $Fm\bar{3}m$ , lattice parameter  $a = 0.4611$  nm) and are indexed as  $\{111\}$ ,  $\{220\}$  and  $\{311\}$ , respectively. Besides, the other diffraction ring is assigned to belong to  $\{110\}$  crystal plane of the metallic molybdenum (Mo) (PDF no. 65-7442, space group  $Im\bar{3}m$ ,  $a = 0.3147$  nm). The left-down inset in Fig. 6b displays the corresponding HRTEM image. The periodic fringe spacing of  $\sim 0.22$  nm corresponds to the interplanar spacing of the  $\{110\}$  plane from metallic Mo, revealing the presence of metallic Mo nanoparticles with an average size of about 5 nm. These results are in line with the CV results (Fig. 4), *i.e.*, the partially lithiated intermediate  $\text{Li}_{0.98}\text{MoO}_2$  phase finally decompose into metallic Mo and  $\text{Li}_2\text{O}$  at voltage less than 0.5 V. The related electrochemical reaction can be described as Eq. (2):

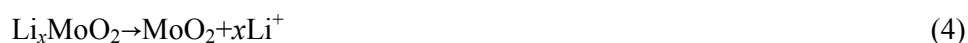


Fig. 6c is a typical TEM observation of the electrode charged to 1.6 V in the first cycle, and the corresponding SAED pattern and HRTEM image are inset. The diffraction rings can be indexed as  $\{011\}$ ,  $\{002\}$ ,  $\{\bar{1}22\}$  and  $\{031\}$  of the monoclinic  $\text{Li}_{0.98}\text{MoO}_2$ , respectively. The HRTEM image (left-down inset) shows the  $\{011\}$  plane of monoclinic  $\text{Li}_{0.98}\text{MoO}_2$  phase, which further prove the presence of intermediate  $\text{Li}_{0.98}\text{MoO}_2$  phase. The analysis here suggests that the metallic Mo oxidize into high

valence intermediate  $\text{Li}_{0.98}\text{MoO}_2$  phase when the electrode is charged to 1.6 V. The related electrochemical reaction can be described as Eq. (3):



Fig. 6d displays a typical TEM image and the corresponding SAED pattern of the electrode charged to 3.0 V in the first cycle. As shown in the figure, the presence of three weak rings (in right-up inset) can be indexed to be  $\{011\}$ ,  $\{\bar{2}11\}$  and  $\{\bar{2}12\}$  of monoclinic  $\text{MoO}_2$  phase. The weak diffractions also suggests that the sample loses its crystallinity after a full lithium uptake/removal process, and ultra fine nanostructured  $\text{MoO}_2$  clusters may exist at the end of lithium removal process. The re-appearance of nanostructured  $\text{MoO}_2$  can be further confirmed by the HRTEM investigation as shown in left-down inset in Fig. 6d. The lattice fringe with spacing of 0.32 nm in the HRTEM image of delithiation product can be assigned to the  $\{011\}$  plane of monoclinic  $\text{MoO}_2$  phase. The results prove the claim that partially lithiated  $\text{Li}_{0.98}\text{MoO}_2$  phase will remove about 1 unit of Li and restore to the monoclinic  $\text{MoO}_2$  phase at 3.0 V. The related electrochemical reaction can be described as Eq. (4):



In order to get more in-depth investigation into the respectable electrochemical performance of thin film electrode, the phase and microstructure evolution of the  $\text{MoO}_2$  thin film electrodes at the 12<sup>th</sup> discharged/charged states were also investigated by using TEM. The bright field image and the corresponding SAED pattern of 0.01 V at 12<sup>th</sup> cycle are shown in Fig. 7a. In the SAED pattern, diffraction rings, come from  $\text{Li}_2\text{O}$  and metallic Mo can be detected, and they can be indexed as  $\{111\}$ ,  $\{220\}$  and

{311} of  $\text{Li}_2\text{O}$  and {110} of the metallic molybdenum, respectively. In the HRTEM image, periodic fringes corresponding to the {110} plane of metallic Mo and {111} plane of  $\text{Li}_2\text{O}$  could be detected, respectively, revealing the presence of metallic Mo nanoparticles and  $\text{Li}_2\text{O}$  phase. They are similar to those observed at the first discharged state as shown in Fig. 6b. Fig. 7b displays a typical TEM image and the corresponding SAED pattern originating from 3 V charged state at the 12<sup>th</sup> cycle. The weak rings shown in Fig. 7b can be indexed to the {011},  $\{\bar{2}11\}$ ,  $\{\bar{1}22\}$ ,  $\{\bar{3}11\}$  and  $\{\bar{4}02\}$  planes of monoclinic  $\text{MoO}_2$  phase. The two lattice fringes in the HRTEM are detected to be about 0.32 nm and 0.23 nm, which belong to the {011} and  $\{\bar{2}11\}$  planes of monoclinic  $\text{MoO}_2$  phase. The phase and microstructure results at 12<sup>th</sup> cycle are in line with the first cycle, which suggests that the electrode is highly reversible and stable during the electrochemical cycles.

It is confirmed that  $\text{MoO}_2$  thin film prepared by RF sputtering are electrochemically activated, so the conversion reaction is thermodynamic and kinetic feasible. Base on the above analysis, it is suggested that a conversion reaction involves during the lithium uptake/removal process as shown in Eqs. (1)~(4), and can also be summarized as  $\text{MoO}_2 + x\text{Li}^+ \leftrightarrow \text{Li}_x\text{MoO}_2 \leftrightarrow \text{Mo} + x\text{Li}_2\text{O}$ . The microstructure evolutions are stepwise, lithiated phase such as  $\text{Li}_{0.98}\text{MoO}_2$  phase is formed before further decomposing into metallic Mo and  $\text{Li}_2\text{O}$  nanoparticles upon the discharging, while during the charging process is in reverse order. Reducing particle size can facilitate the conversion reaction of the  $\text{MoO}_2$  thin film electrode due to the enlargement of surface area, thus enhancing the charge transfer reaction and solid

state Li ion diffusion.

#### 4. Conclusions

MoO<sub>2</sub> thin film has been successfully synthesized *via* RF sputtering method. The as deposited MoO<sub>2</sub> thin film has hierarchical structure with a great deal of micro-sized cauliflower-like humps composed of hundreds of nano-sized particles with dispersed nano domains and disordered domain boundaries. As an electrode for lithium ion battery, the MoO<sub>2</sub> thin film exhibits a high specific capacity, fantastic cycling performance and the excellent rate performance. The significant enhancement in the electrochemical lithium ion storage performance of MoO<sub>2</sub> thin film is attributable to the ultra fine nano domain, binder and carbon free preparation. TEM results confirm that the MoO<sub>2</sub> thin film electrodes undergo a conversion reaction that can be summarized as  $\text{MoO}_2 + x\text{Li}^+ \leftrightarrow \text{Li}_x\text{MoO}_2 \leftrightarrow \text{Mo} + x\text{Li}_2\text{O}$ .

#### Acknowledgments

The authors acknowledge the support of the National Nature Science Foundation of China (No. 51172287) and the Laboratory Research Fund by the State Key Laboratory of Powder Metallurgy, China.

#### Notes and References

1. J. B. Goodenough and Y. Kim, *Chem. Mater.*, 2010, **22**, 587.
2. M. S. Whittingham, *MRS Bull.*, 2008, **33**, 411.
3. V. Etacheri, R. Marom, R. Elazari, G. Salitra and D. Aurbach, *Energy Environ. Sci.*, 2011, **4**, 3243.
4. L. W. Ji, Z. Lin, M. Alcoutlabi and X. W. Zhang, *Energy Environ. Sci.*, 2011, **4**, 2682.

5. Y. Si, T. Ren, B. Ding, J. Yu and G. Sun, *J. Mater. Chem.*, 2012, **22**, 4619.
6. G. P. Kim, S. Park, I. Nam, J. Park and J. Yi, *J. Mater. Chem. A*, 2013, **1**, 3872.
7. X. Wang, L. Qiao, X. Sun, X. Li, D. Hu, Q. Zhang and D. He, *J. Mater. Chem. A*, 2013, **1**, 4173.
8. M. A. Lowe, J. Gao and H. D. Abruña, *J. Mater. Chem. A*, 2013, **1**, 2094.
9. Y. L. Liu, H. Zhang, P. Ouyang and Z. C. Li, *Electrochim. Acta*, 2013, **102**, 429.
10. X. Zhang, X. Song, S. Gao, Y. Xu, X. Cheng, H. Zhao and L. Huo, *J. Mater. Chem. A*, 2013, **1**, 6858.
11. Y. M. Sun, X. L. Hu, W. Luo and Y. H. Huang, *ACS Nano*, 2011, **5**, 7100.
12. F. F. Xia, X. L. Hu, Y. M. Sun, W. Luo and Y. H. Huang, *Nanoscale*, 2012, **4**, 4707.
13. A. Bhaskar, M. Deepa, T. N. Rao and U. V. Varadaraju, *J. Power Sources*, 2012, **216**, 169.
14. Z. Y. Wang, J. S. Chen, T. Zhu, S. Madhavi and X. W. Lou, *Chem. Commun.*, 2010, **46**, 6906.
15. Y. F. Shi, B. K. Guo, S. A. Corr, Q. H. Shi, Y. S. Hu, K. R. Heier, L. Q. Chen, R. Seshadri and G. D. Stucky, *Nano Lett.*, 2009, **9**, 4215.
16. B. K. Guo, X. P. Fang, B. Li, Y. F. Shi, C. Y. Ouyang, Y.-S. Hu, Z. X. Wang, G. D. Stucky and L. Q. Chen, *Chem. Mater.*, 2011, **24**, 457.
17. L. C. Yang, Q. S. Gao, Y. Tang, Y. P. Wu and R. Holze, *J. Power Sources*, 2008, **179**, 357.
18. J. P. Pereira-Ramos, N. Kumagai and N. Kumagai, *J. Power Sources*, 1995, **56**, 87.
19. A. Manthiram and C. Tsang, *J. Electrochem. Soc.*, 1996, **143**, L143.
20. J. H. Ku, Y. S. Jung, K. T. Lee, C. H. Kim and S. M. Oh, *J. Electrochem. Soc.*, 2009, **156**, A688.
21. D. Larcher, G. Sudant, J. Leriche, Y. Chabre and J. Tarascon, *J. Electrochem. Soc.*, 2002, **149**, A234.
22. Y. L. Liu, H. Zhang, P. Ouyang, W. H. Chen and Z. C. Li, *Mater. Res. Bull.*, 2014, **50**, 95.
23. H. Li, P. Balaya and J. Maier, *J. Electrochem. Soc.*, 2004, **151**, A1878.
24. L. C. Yang, Q. S. Gao, Y. H. Zhang, Y. Tang and Y. P. Wu, *Electrochem. Commun.*, 2008, **10**, 118.
25. X. Li, J. Yang, Y. Hu, J. Wang, Y. Li, M. Cai, R. Li and X. Sun, *J. Mater. Chem.*, 2012, **22**, 18847.
26. C. Ban, Z. Wu, D. T. Gillaspie, L. Chen, Y. Yan, J. L. Blackburn and A. C. Dillon, *Adv. Mater.*, 2010, **22**, E145.
27. D.-H. Ha, M. A. Islam and R. D. Robinson, *Nano Lett.*, 2012, **12**, 5122.
28. Z.-W. Fu, Y. Wang, Y. Zhang and Q.-Z. Qin, *Solid State Ionics*, 2004, **170**, 105.
29. C.-M. Hwang and J.-W. Park, *Electrochim. Acta*, 2011, **56**, 6737.
30. W.-J. Li and Z.-W. Fu, *Appl. Surf. Sci.*, 2010, **256**, 2447.
31. Q. Shi, J. Liu, R. Hu, M. Zeng, M. Dai and M. Zhu, *RSC Advances*, 2012, **2**, 7273.
32. R. Hu, H. Liu, M. Zeng, J. Liu and M. Zhu, *J. Mater. Chem.*, 2012, **22**, 9539.
33. Z.-W. Fu, J. Ma and Q.-Z. Qin, *Solid State Ionics*, 2005, **176**, 1635.
34. M. Balasubramanian, X. Sun, X. Yang and J. McBreen, *J. Power Sources*, 2001, **92**, 1.
35. F. Kong, R. Kostecki, G. Nadeau, X. Song, K. Zaghib, K. Kinoshita and F. McLarnon, *J. Power Sources*, 2001, **97**, 58.
36. D. Chen, S. Indris, M. Schulz, B. Gamer and R. Mönig, *J. Power Sources*, 2011, **196**, 6382.
37. Y.-L. Kim, Y.-K. Sun and S.-M. Lee, *Electrochim. Acta*, 2008, **53**, 4500.
38. G. C. Bond, S. Flamerz, L. Van Wijk, *Catal. Today*, 1987, **1**, 229.
39. X. Y. Chen, Z. J. Zhang, X. X. Li, C. W. Shi, X. L. Li, *Chemical Physics Letters*, 2006, **418**, 105.
40. R. Dedryvère, S. Laruelle, S. Grugeon, P. Poizot, D. Gonbeau and J. M. Tarascon, *Chem. Mater.*, 2004, **16**, 1056.
41. J. R. Dahn and W. R. McKinnon, *Solid State Ionics*, 1987, **23**, 1.

42. S. H. Lee, Y. H. Kim, R. Deshpande, P. A. Parilla, E. Whitney, D. T. Gillaspie, K. M. Jones, A. Mahan, S. Zhang and A. C. Dillon, *Adv. Mater.*, 2008, **20**, 3627.
43. J. H. Ku, J. H. Ryu, S. H. Kim, O. H. Han and S. M. Oh, *Adv. Funct. Mater.*, 2012, **22**, 3658-3664.
44. J. Maier, *Nature materials*, 2005, **4**, 805.
45. P. Balaya, A. J. Bhattacharyya, J. Jamnik, Y. F. Zhukovskii, E. A. Kotomin and J. Maier, *J. Power Sources*, 2006, **159**, 171.
46. F. Xia, X. Hu, Y. Sun, W. Luo and Y. Huang, *Nanoscale*, 2012, **4**, 4707.
47. X. Y. Zhao, M. H. Cao, B. Liu, Y. Tian and C. W. Hu, *J. Mater. Chem.*, 2012, **22**, 13334.
48. Y. Sun, J. Wang, B. Zhao, R. Cai, R. Ran and Z. Shao, *J. Mater. Chem. A*, 2013, **1**, 4736.
49. Y. M. Sun, X. L. Hu, W. Luo and Y. H. Huang, *J. Mater. Chem.*, 2012, **22**, 425.

## Figure Captions

**Figure 1.** SEM observations of the as-deposited MoO<sub>2</sub> thin film on the Cu foil substrate. The inset (a) is a SEM image of the Cu foil surface, exhibiting nodule type structure with numerous micro columnar; the inset (b) is a secondary electron image of the surface characteristic of an as-deposited MoO<sub>2</sub> thin film; the inset (c) shows an enlarged view of the surface of an as-deposited MoO<sub>2</sub> thin film; the inset (d) shows a cross-sectional SEM observation of an as-deposited MoO<sub>2</sub> thin film.

**Figure 2.** Investigations of phase component, electronic state and chemical composition of the as-deposited MoO<sub>2</sub> thin films, (a) XRD analysis of the thin film on silicon substrate, (b) XPS spectrum for the thin film deposited on glass, and (c) high resolution XPS of Mo 3d.

**Figure 3.** Microstructure investigations of the as-deposited MoO<sub>2</sub> thin films. (a) low magnification TEM image and inset the related SAED diffraction, (b) high resolution TEM image.

**Figure 4.** Cyclic voltammograms of a MoO<sub>2</sub> thin film electrode induced at 1<sup>st</sup>, 2<sup>nd</sup>, 5<sup>th</sup> and 100<sup>th</sup> cycles.

**Figure 5.** Electrochemical characteristics of the MoO<sub>2</sub>-based thin film electrode. (a) galvanostatic discharge-charge profiles recorded in the range of 0.01-3 V, at a current rate of 400 mA g<sup>-1</sup>, (b) differential capacity curves, (c) cycling performance at a current rate of 400 mA g<sup>-1</sup>, (d) rate performance at the current rates of 400 mA g<sup>-1</sup> to 800 mA g<sup>-1</sup>, 1600 mA g<sup>-1</sup> and 3200 mA g<sup>-1</sup>, respectively.

**Figure 6.** TEM investigations of MoO<sub>2</sub> thin film electrodes discharged/charged to various stages in the first electrochemical cycle, (a) discharged to 1.3 V, (b) discharged to 0.01 V, (c) charged to 1.6 V, (d) charged to 3.0 V.

**Figure 7.** TEM investigations of MoO<sub>2</sub> thin film electrodes after being induced at different discharged/charged states at the 12<sup>th</sup> electrochemical cycle, (a) bright field image and corresponding SAED pattern when discharged to 0.01 V, (b) TEM image and corresponding SAED pattern originating from 3 V charged state.

Figure 1

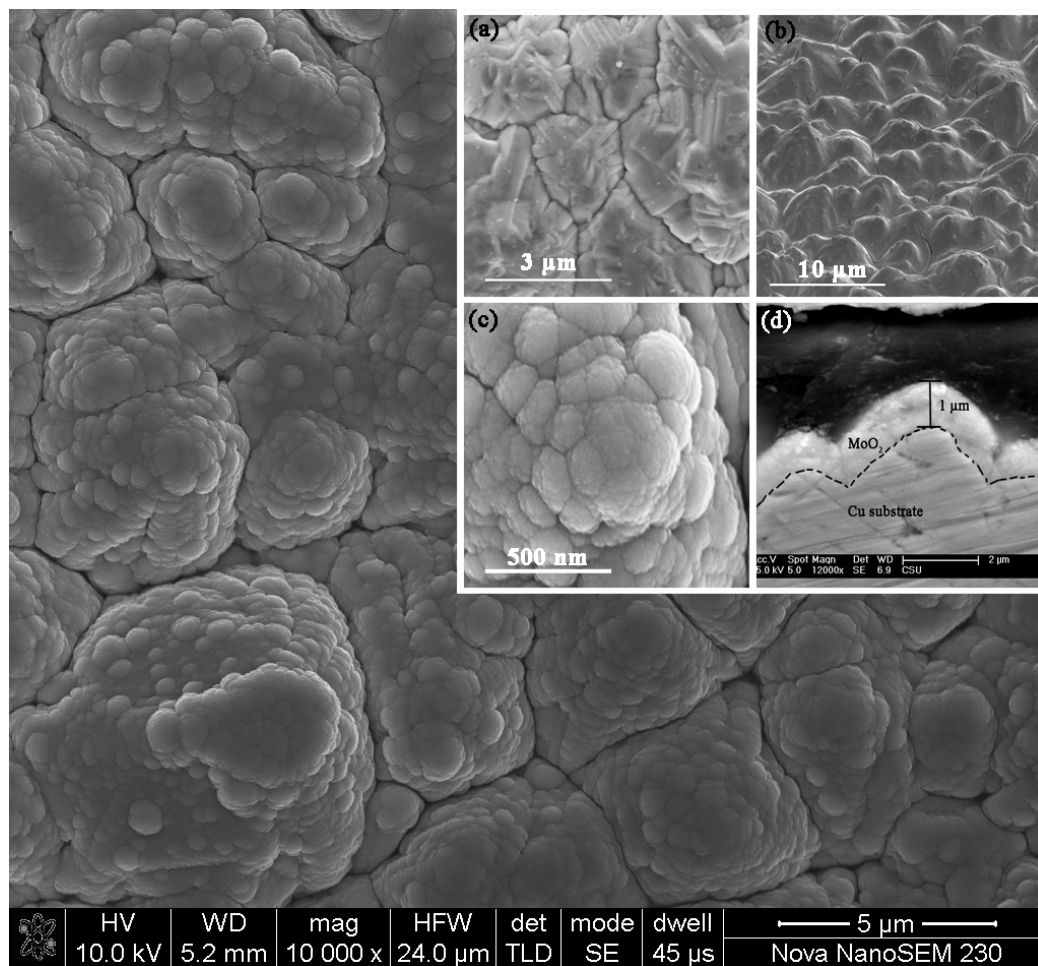
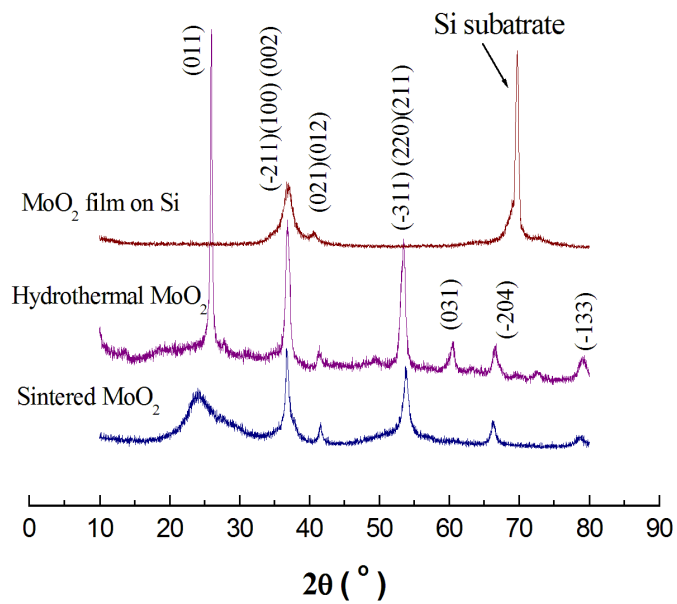
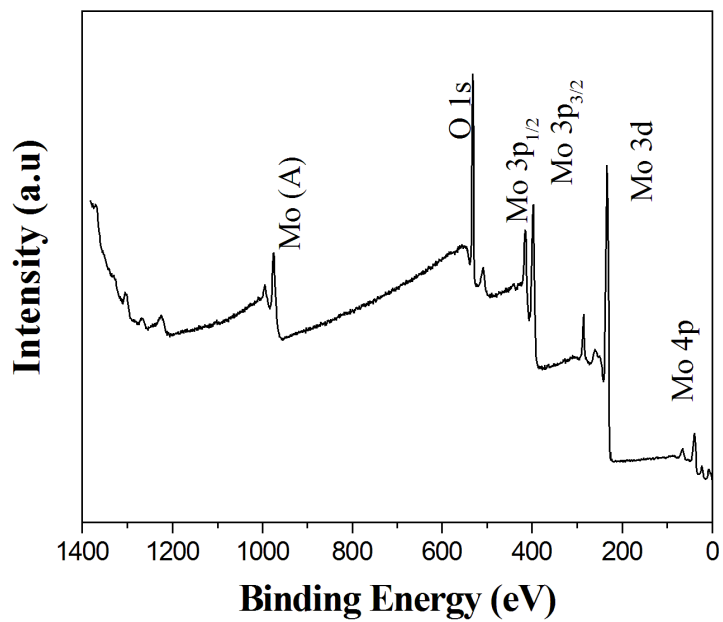


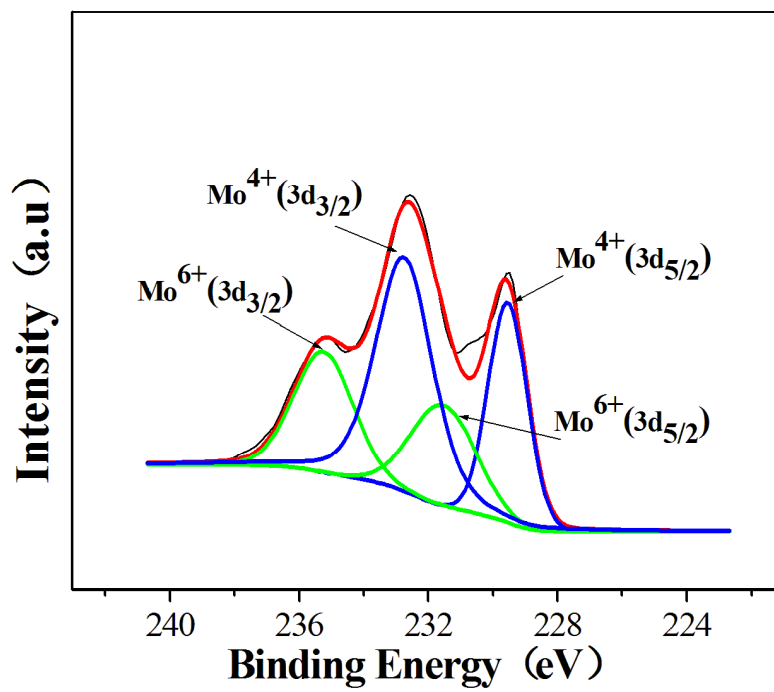
Figure 2



(a)

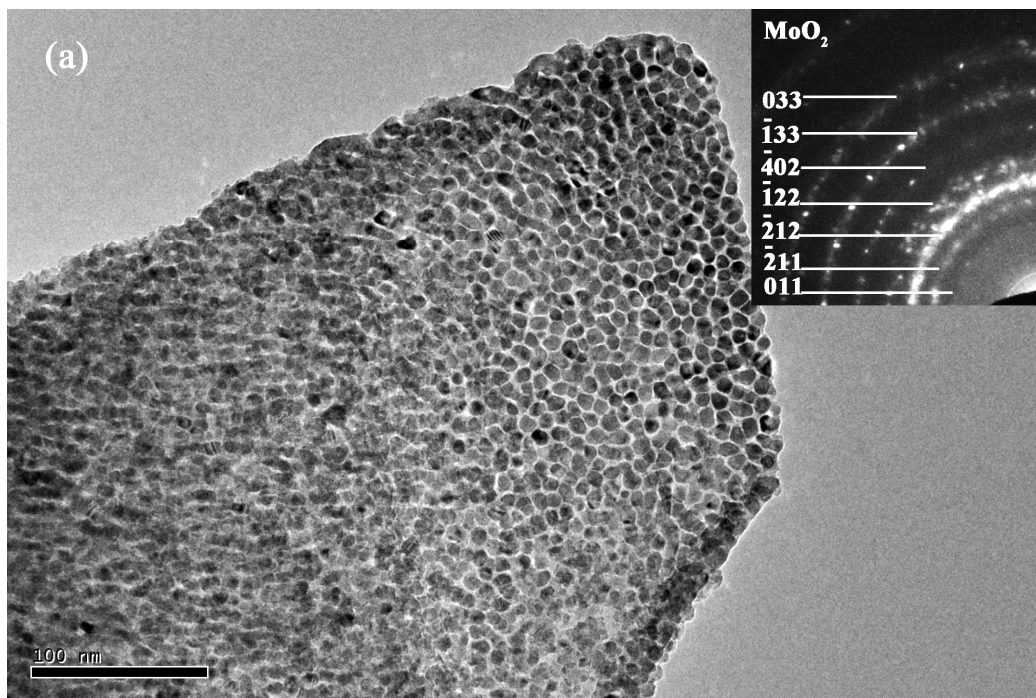


(b)

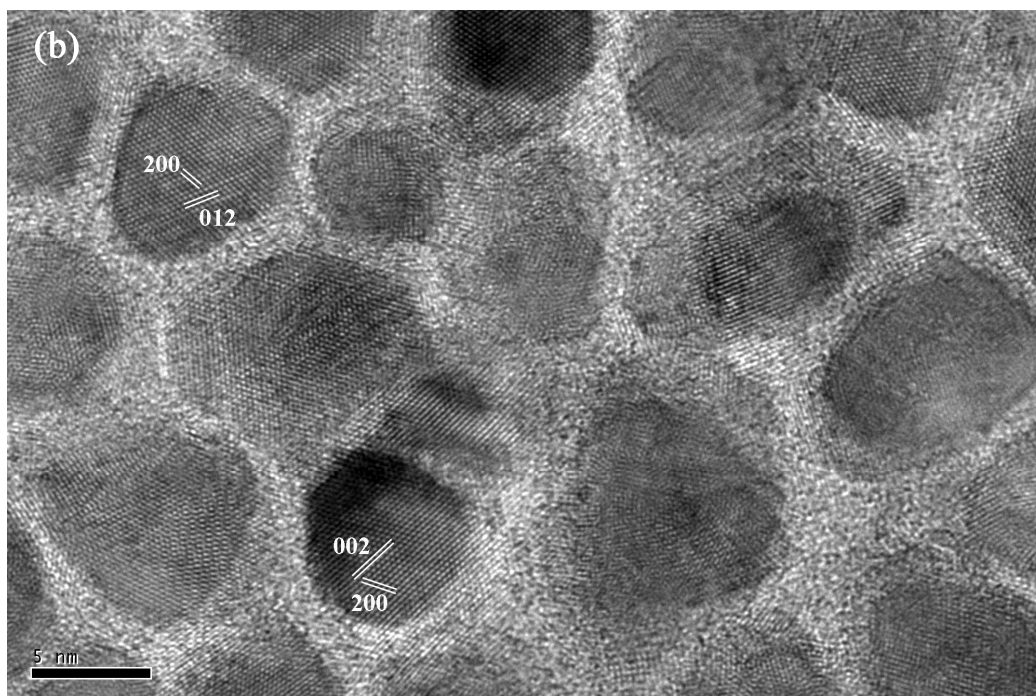


(c)

Figure 3



(a)



(b)

Figure 4

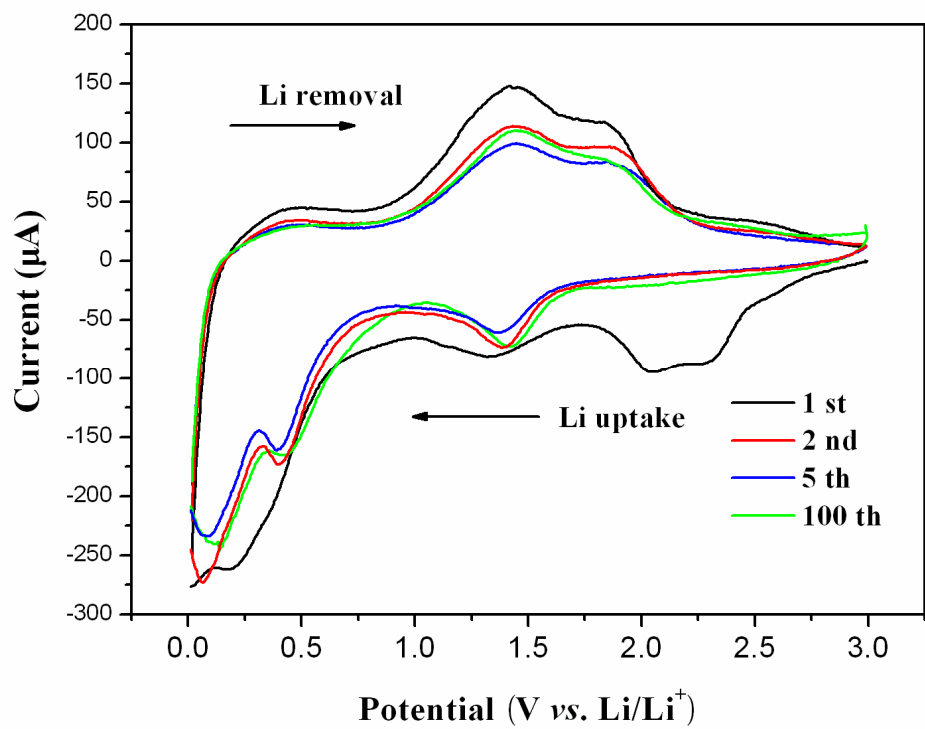
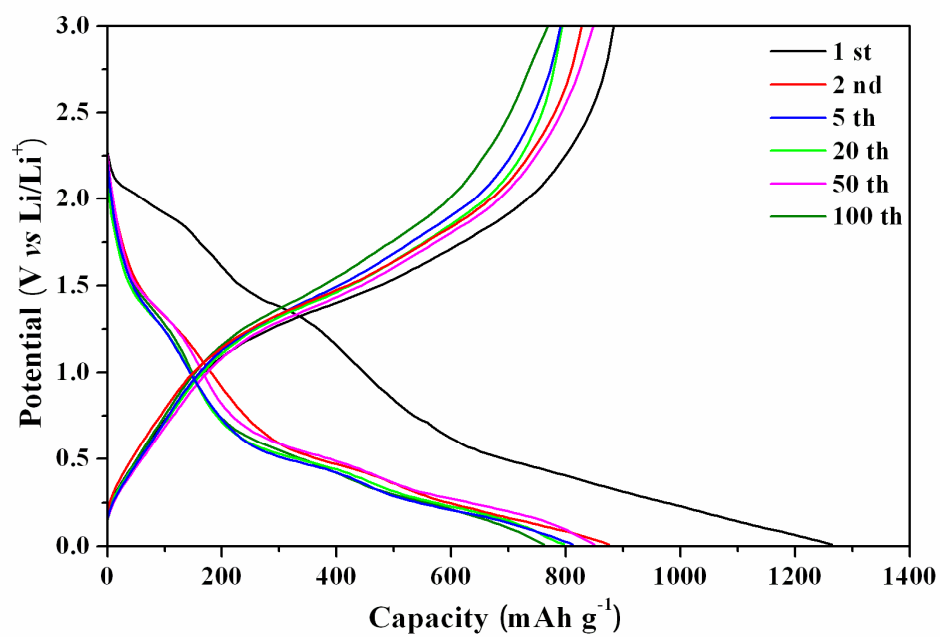
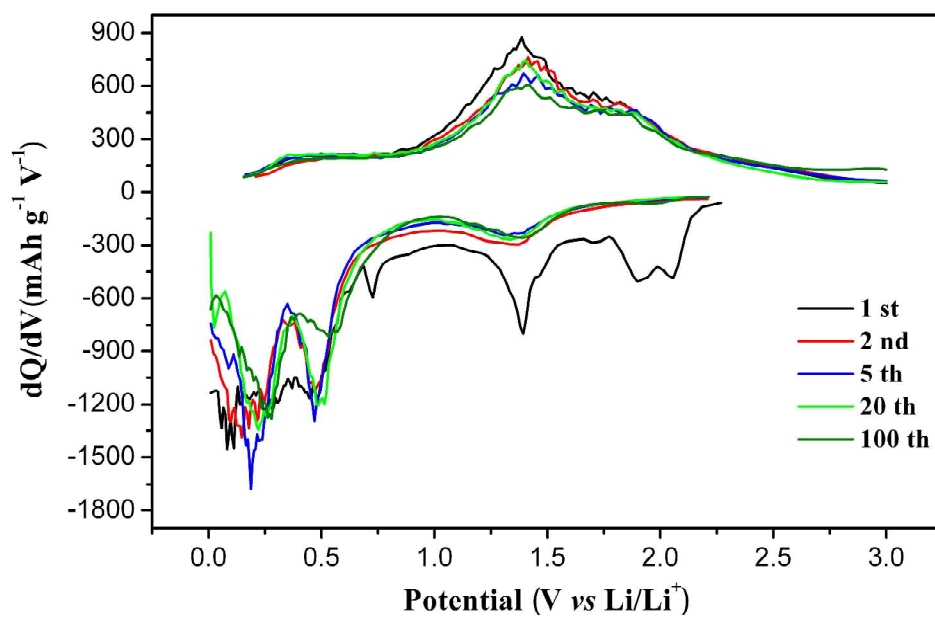


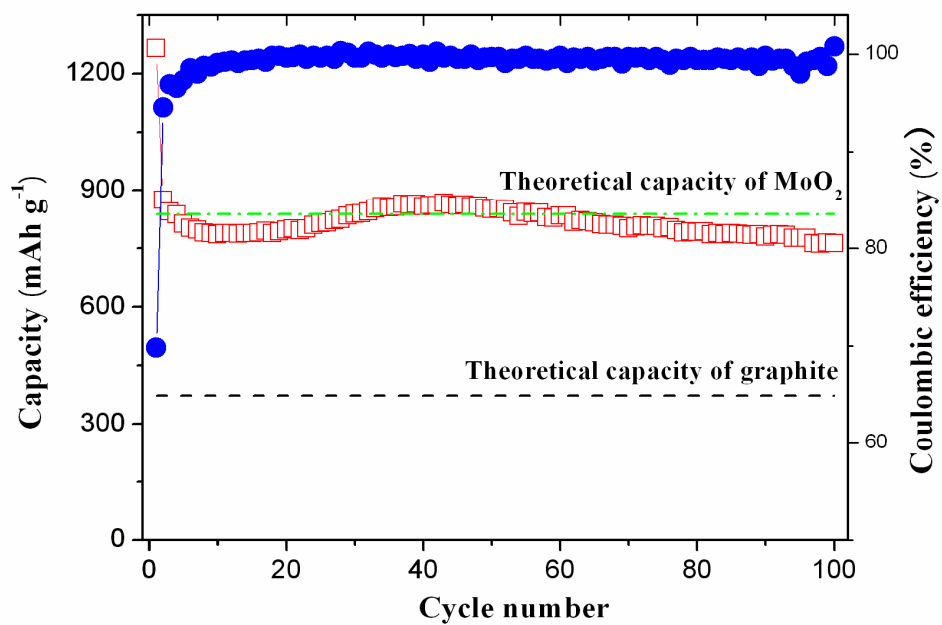
Figure 5



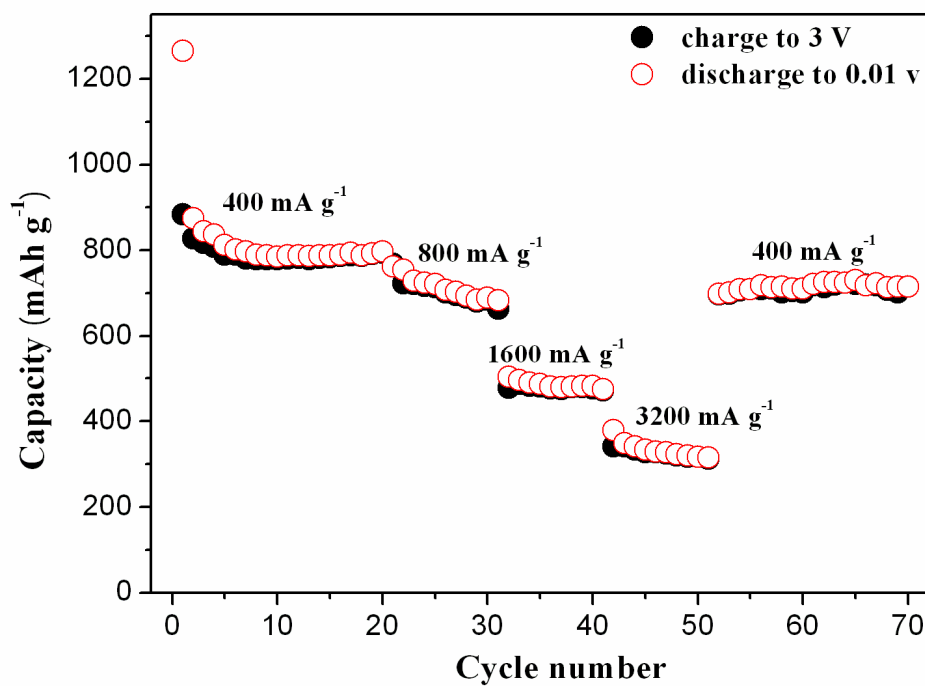
(a)



(b)

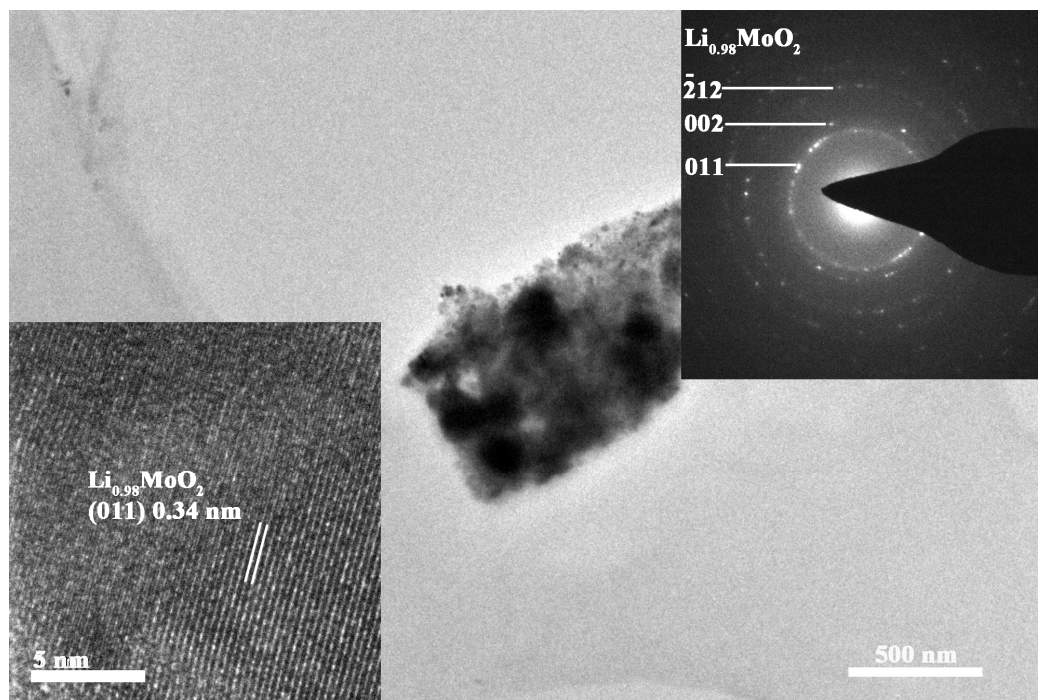


(c)

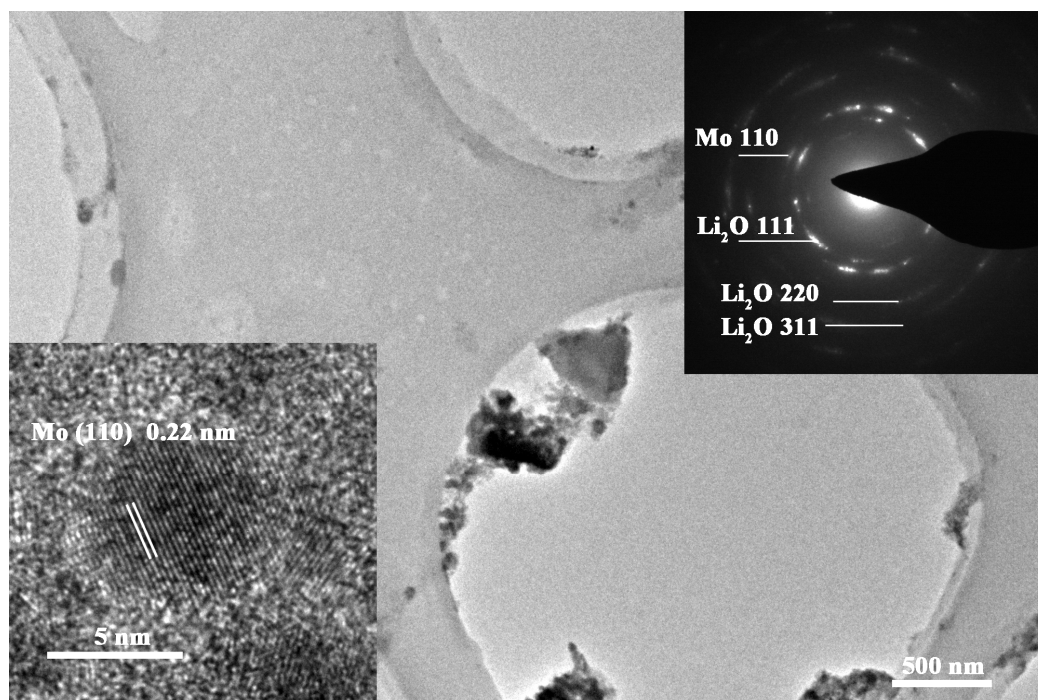


(d)

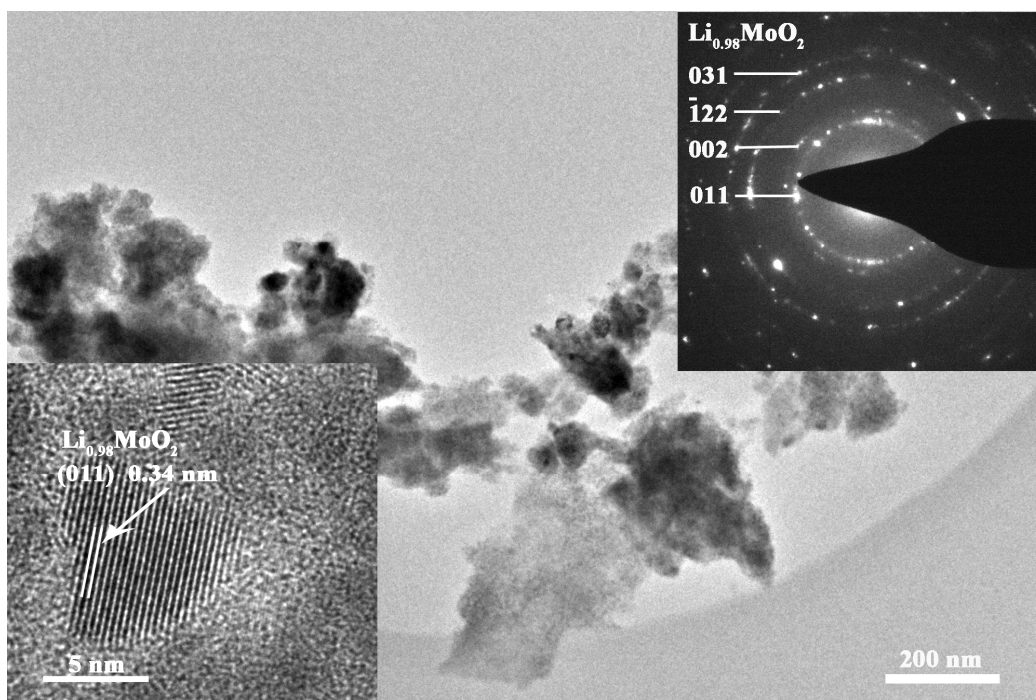
Figure 6



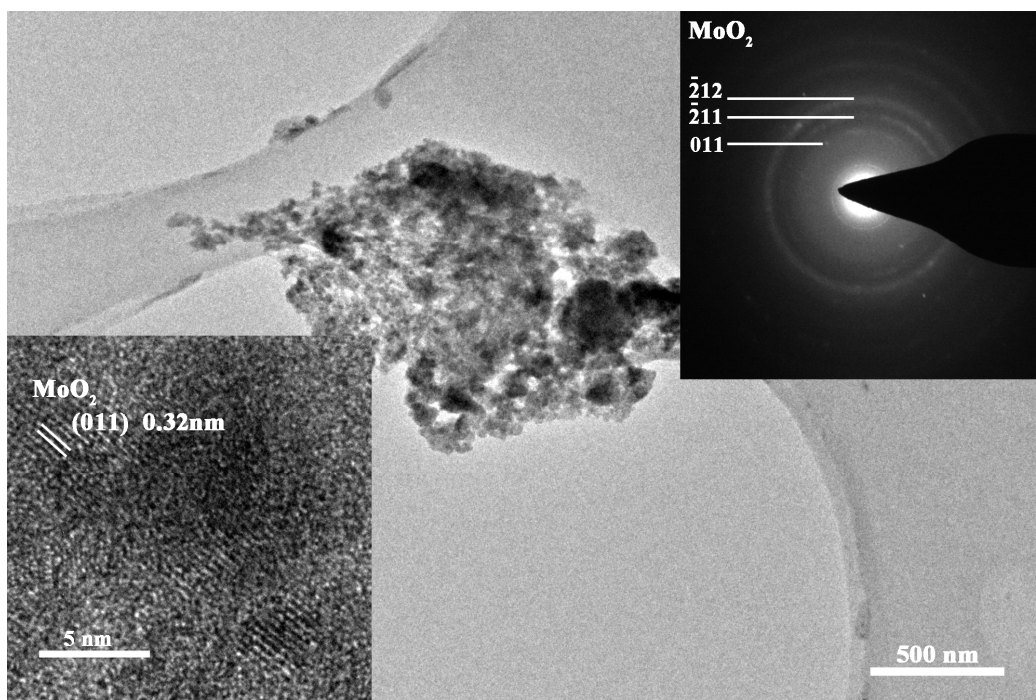
(a)



(b)

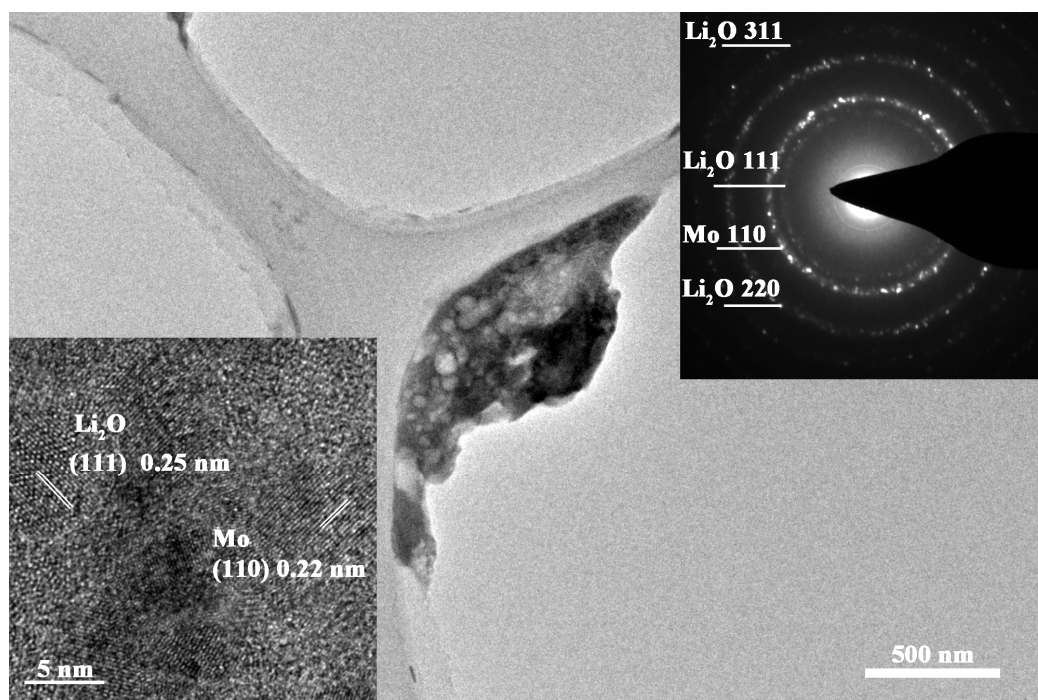


(c)

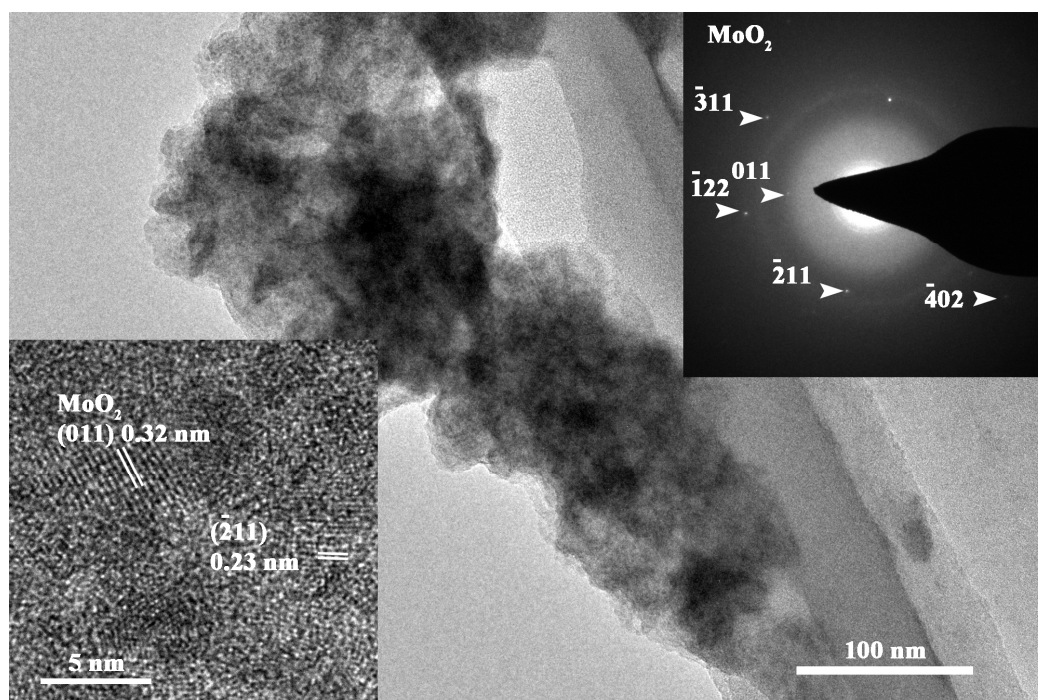


(d)

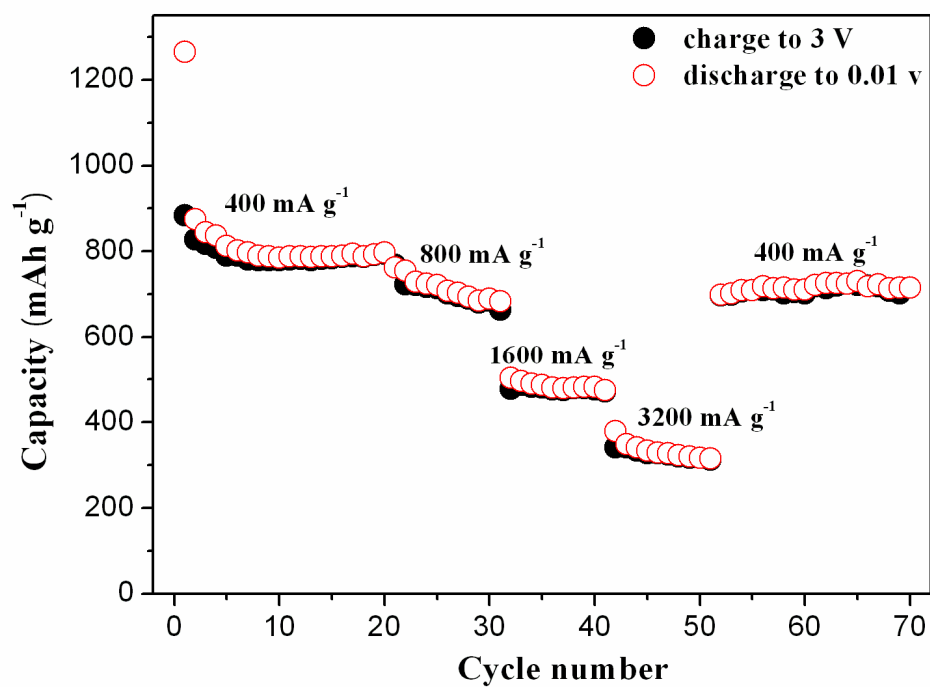
Figure 7



(a)



(b)



MoO<sub>2</sub> thin film with hierarchical structure demonstrates excellent rate capability and reversible capacity, and the phase transformation mechanism was revealed.